

Excitation of weak and strong guided waves in a semiconductor slab and their strong coupling with confined magnetoexcitons

P. L. Valdés-Negrin ¹, N. M. Makarov ^{2,*} and F. Pérez-Rodríguez ^{1,†}

¹*Instituto de Física, Benemérita Universidad Autónoma de Puebla, Puebla, Pue. 72570, México*

²*Instituto de Ciencias, Benemérita Universidad Autónoma de Puebla, Puebla, Pue. 72570, México*



(Received 27 September 2021; revised 5 May 2022; accepted 13 June 2022; published 23 June 2022)

We have obtained and analyzed optical spectra of a semiconductor slab, containing a quantum well which serves as a source of magnetoexcitons in the presence of an external dc magnetic field. Our setup corresponds to the optical technique based on the breaking of the total internal reflection. Specifically, the semiconductor slab is sandwiched between two external leads/prisms separated from the slab by two gap layers of a dielectric or metal. The reflectivity, transmissivity, and absorption spectra for such a system in a quantizing magnetic field were revealed to display a resonant structure originating from the excitation of electromagnetic modes localized on the semiconductor slab which are strongly coupled with the confined magnetoexcitons. It is surprising that the Rabi splitting for the setup with dielectric gap layers (weak guiding) turns out to be greater than that for metallic and even semiconductor microcavities (strong guiding). Our results were verified by comparing the calculated optical spectra with the dispersion curves for localized modes derived analytically.

DOI: [10.1103/PhysRevB.105.245309](https://doi.org/10.1103/PhysRevB.105.245309)

I. INTRODUCTION

Adjusting light-matter interactions offers an improvement in efficiency of devices and the development of unique applications [1]. Depending on the strength of the coupling, several different regimes can be established [2]: weak, strong, very strong, and ultrastrong coupling. In semiconductor microcavities, the weak coupling regime occurs when the measure of coupling between the electromagnetic field and a crystal quasiparticle (e.g., exciton) is smaller than the width of the cavity mode and is characterized by an irreversible decay [3]. The presence of the microcavity modifies the radiative decay rate of the exciton [4]. The strong coupling regime emerges when the light-matter coupling is larger than the decay rate and no irreversible decay takes place: instead, the energy oscillates between the exciton and photon modes (Rabi oscillations), leading to a Rabi splitting in the frequency domain [5,6]. The latter manifests itself in the appearance of two eigenmodes, namely, the lower (LP) and upper (UP) polaritons, which are linear superpositions of the bare exciton and photon states. At zero detuning, i.e., when exciton and photon energies coincide, the LP and UP are separated by the Rabi splitting. The strong coupling between excitons and photons in planar semiconductor microcavities has been studied experimentally and theoretically [7–10]. If the measure of coupling is comparable with the exciton binding energy, the regime is called very strong coupling and is distinguished by the appearance of different hybridized excitons levels since the wave function of the electron-hole pair is effectively modified [11,12]. Finally, in the ultrastrong coupling regime,

hybridized states with different numbers of excitations are observed [13–16].

The strong coupling of excitons with photons can also be achieved in metal microcavities [17–21]. The use of metal mirrors offers the advantage that they serve as electrodes, allowing electrical excitation of the polaritons in the cavity [18,21]. In addition, the penetration depth in metal mirrors is smaller than in distributed Bragg reflectors (DBRs) of semiconductor microcavities and, therefore, the photon confinement in metallic microcavities is stronger than that in semiconductor ones. For this reason, larger Rabi splitting energies for metallic microcavities have been experimentally demonstrated [17].

It has been shown that strong coupling between waveguide modes and excitonic states can be realized in dye molecules [22] and quantum wells (QWs) [23]. In particular, the strong coupling of inorganic QW excitons to the guided modes of a planar film waveguide was reported in Ref. [24]. In Ref. [25], the waveguided polaritons on a III-nitride slab with *c*-plane GaN/(Al,Ga)N QWs was studied in the strong coupling regime. Excitons in semiconductor nanowires can also be *strongly* coupled to *weakly* guided photons [26,27], i.e., when the wires are surrounded by a medium with lower refractive index. Recently, the strong-coupling regime between electromagnetic modes guided by a semiconductor nanowire and excitonic states of molecules localized in its surrounding media was predicted in Ref. [28]. The fact of using a slab surrounded by a dielectric medium instead of a semiconductor microcavity offers an advantage in experimental design for reducing the number of layers. On the other hand, the substitution of metallic layers in a metallic microcavity by dielectric media could considerably reduce the losses in the system.

In the presence of an external strong dc magnetic field, the QW exciton changes into a different quasiparticle, the

*makarov.n@gmail.com

†fperez@ifuap.buap.mx

so-called magnetoexciton. To the best of our knowledge, the strong coupling of light with magnetoexcitons in a semiconductor QW has only been theoretically studied in semiconductor microcavities [29,30]. The impact of the coupling between magnetoexciton and waveguide modes in a semiconductor QW embedded either in a dielectric or in metal is an open question. Furthermore, the optical excitation itself of magnetoexcitons in such nanostructures is also of relevant interest. A possible technique for the excitation of magnetoexcitons coupled to waveguide modes can be that based on breaking the total internal reflection (TIR) with the use of two prisms. It should be mentioned that such an optical technique has been recently applied for exciting THz electromagnetic localized Josephson plasma waves in a superconducting slab with internal insulating layers perpendicular [31,32] and parallel [33] to its surfaces.

In the present paper, we develop a unified formalism for theoretically studying the excitation of waveguide modes localized on a semiconductor waveguide and the emergence of strong-coupling regimes between guided modes and magnetoexciton states. Here we shall consider a semiconductor slab with a QW being covered either by two dielectrics or by two metal layers, which are adjacent to two prisms. The developed formalism is based on the Stahl-Balslev real-space density-matrix approach [34], which employs a system of coupled equations for the coherent-wave amplitude and the electromagnetic fields in the semiconductor slab. Such a formalism has been successfully employed for studying the coupling of photons with magnetoexcitons in semiconductor QW heterostructures [29,30,35–38].

The paper is organized as follows. In Secs. II and III, we formulate the problem, present the system geometry, and introduce the basic definitions and notations. In addition, in Sec. III, we briefly elucidate the origin of localized eigenmodes. Then, we calculate and analyze s -polarized optical spectra for the semiconductor slab covered by dielectrics, Sec. IV, as well as metal, Sec. V. In the analysis, the dispersion relation of the electromagnetic modes localized on the semiconductor slab is used to interpret the features of optical spectra. In Sec. VI, the strong coupling of magnetoexcitons with guided modes, observed in the optical spectra, is compared with the optical manifestation of magnetoexcitons in semiconductor microcavities with the QW. There is a section of conclusions, Sec. VII.

II. MODEL FORMULATION

Let us consider an electromagnetic wave propagating through a semiconductor slab c consisting of a cap layer ($0 < x < x_1$), a semiconductor QW ($x_1 < x < x_2$), and a buffer layer ($x_2 < x < d_c$). The semiconductor slab c is under the action of an external dc magnetic field \mathbf{B}_0 applied perpendicularly to the slab along the x axis ($\mathbf{B}_0 \parallel \mathbf{x}$). The propagation should be accompanied by the resonant excitation of waveguide modes localized on the slab that is achieved with the use of the setup depicted schematically in Fig. 1. Specifically, the semiconductor slab c is placed between two identical semi-infinite dielectric leads, a_L and a_R , with positive permittivity $\varepsilon_a > 0$ and separated from them by two gap layers, b_L and b_R , of permittivity ε_b and thickness d_b . An incident electromag-

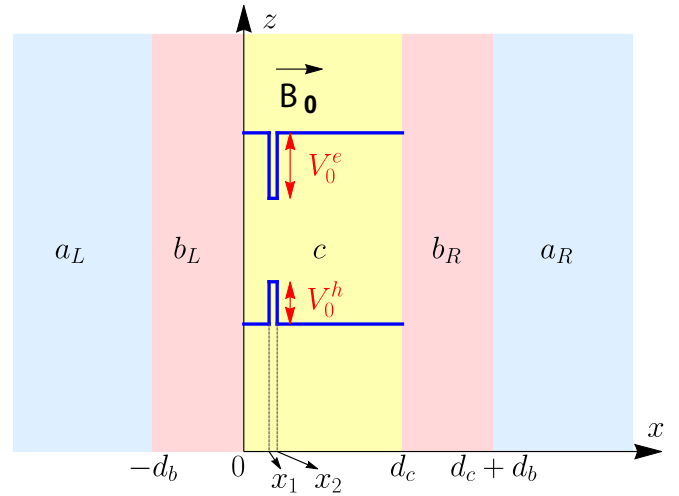


FIG. 1. A sketch of the setup and the coordinate system. The valence and conduction band edges for the QW heterostructure is defined by the electron/hole steplike confining potential (upper/lower blue curves, respectively). The dc magnetic field \mathbf{B}_0 is oriented perpendicular to the QW plane.

netic wave comes onto interface ($a_L|b_L$) from the left lead a_L , while the right lead a_R serves as a receiver of a transmitted wave going out from interface ($b_R|a_R$).

Throughout our paper, the resonant transmission phenomenon is analyzed for the electromagnetic waves of TE polarization (or the same of s polarization). In line with the chosen coordinate system, this fact implies the electric $\mathbf{E}(x, z, t)$ and magnetic $\mathbf{H}(x, z, t)$ fields to be expressed as

$$\mathbf{E}(x, z, t) = \{0, E_y(x), 0\} \exp(ik_z z - i\omega t), \quad (2.1a)$$

$$\mathbf{H}(x, z, t) = \{H_x(x), 0, H_z(x)\} \exp(ik_z z - i\omega t). \quad (2.1b)$$

The wave frequency ω and the tangential wave number k_z are assumed to be free external positive parameters of the problem. However, the requirement of wave propagation inside the left/right leads a_L and a_R provides the constitutive restriction

$$k_z < k\sqrt{\varepsilon_a}, \quad k = \omega/c \quad (2.2)$$

should be met.

According to the problem geometry formulated above, the electromagnetic radiation inside the left lead a_L represents a superposition of incident and reflected plane waves, whereas in the right lead a_R there is a transmitted wave only. Specifically,

$$E_y(x) = e^{ik_a(x+d_b)} + A_L^- e^{-ik_a(x+d_b)}, \quad (2.3a)$$

$$H_z(x) = \frac{k_a}{k} \left[e^{ik_a(x+d_b)} - A_L^- e^{-ik_a(x+d_b)} \right] \quad (2.3b)$$

inside semi-infinite medium a_L where $x \leq -d_b$, and

$$E_y(x) = A_R^+ e^{ik_a(x-d_c-d_b)}, \quad (2.4a)$$

$$H_z(x) = \frac{k_a}{k} A_R^+ e^{ik_a(x-d_c-d_b)} \quad (2.4b)$$

inside semi-infinite medium a_R where $d_c + d_b \leq x$. Here, without loss of generality, we have assumed the unit amplitude of the incident wave. The symbols A_L^- and A_R^+ stand for the

reflected and transmitted amplitudes at the interfaces ($a_L|b_L$) and ($b_R|a_R$), respectively. Under the indispensable condition (2.2), the x projection k_a of the wave vector inside leads a_L and a_R is evidently real valued:

$$k_a = \sqrt{k^2 \varepsilon_a - k_z^2}. \quad (2.5)$$

The resonant excitation of waveguide modes localized on the semiconductor slab c is realized when conditions of the TIR at the ($a_L|b_L$) and ($b_R|a_R$) interfaces are satisfied. In such a case, the distribution of electromagnetic field in the gap layers b_L and b_R is described by a linear combination of evanescent waves. Thus,

$$E_y(x) = B_L^+ e^{-\kappa_b x} + B_L^- e^{\kappa_b x}, \quad (2.6a)$$

$$H_z(x) = \frac{i\kappa_b}{k} [B_L^+ e^{-\kappa_b x} - B_L^- e^{\kappa_b x}] \quad (2.6b)$$

inside the left gap layer b_L where $-d_b \leq x \leq 0$, and

$$E_y(x) = B_R^+ e^{-\kappa_b(x-d_c)} + B_R^- e^{\kappa_b(x-d_c)}, \quad (2.7a)$$

$$H_z(x) = \frac{i\kappa_b}{k} [B_R^+ e^{-\kappa_b(x-d_c)} - B_R^- e^{\kappa_b(x-d_c)}] \quad (2.7b)$$

inside the right gap layer b_R where $d_c \leq x \leq d_c + d_b$. The corresponding wave amplitudes at the interfaces ($b_L|c$) and ($c|b_R$) are denoted as B_L^+ , B_L^- and B_R^+ , B_R^- , respectively. Then, in contrast to the wave number k_a , the x projection k_b of the wave vector in the gap layers b_L and b_R must be imaginary:

$$k_b = i\kappa_b, \quad \kappa_b = \sqrt{k_z^2 - k^2 \varepsilon_b}. \quad (2.8)$$

Inside the semiconductor slab c ($0 \leq x \leq d_c$), the electromagnetic field is coupled with a magnetoexciton. The description of this coupling can be adequately realized in terms of the polarization vector $\mathbf{P}(x, z, t)$. For s -polarization Eqs. (2.1) with the chosen geometry of Fig. 1, it is defined as

$$\mathbf{P}(x, z, t) = \{0, P_y(x), 0\} \exp(ik_z z - i\omega t). \quad (2.9)$$

Therefore, the wave electromagnetic field inside the semiconductor QW structure obeys Maxwell equations, which are reduced to

$$\left(\frac{d^2}{dx^2} + k_c^2 \right) E_y(x) = -k^2 P_y(x), \quad (2.10a)$$

$$H_z(x) = \frac{1}{ik} \frac{d}{dx} E_y(x) \quad (2.10b)$$

with the background wave number k_c being defined by

$$k_c = \sqrt{k^2 \varepsilon_c - k_z^2}. \quad (2.11)$$

The transverse wave number k_c is characterized by the background dielectric permittivity $\varepsilon_c > 0$ of the semiconductor slab c without the QW. The general solution of Eq. (2.10a) for the electric field is appropriate to obtain in terms of the quantities $H_z(0)$, $H_z(d_c)$, and $P_y(x)$:

$$\begin{aligned} E_y(x) = & \frac{ik}{k_c} \frac{H_z(0) \cos[k_c(d_c - x)] - H_z(d_c) \cos(k_c x)}{\sin(k_c d_c)} \\ & - \frac{k^2}{k_c} \int_0^x P_y(x') \sin[k_c(x - x')] dx' \\ & - \frac{k^2}{k_c} \frac{\cos(k_c x)}{\sin(k_c d_c)} \int_0^{d_c} P_y(x') \cos[k_c(d_c - x')] dx'. \end{aligned} \quad (2.12)$$

The integration constants $H_z(0)$ and $H_z(d_c)$ determine the tangential wave magnetic field on the semiconductor slab boundaries $x = 0$ and $x = d_c$.

To proceed further, we should calculate polarization $P_y(x)$ and, as a consequence, associate it with the electric field $E_y(x)$. To this end, the Stahl-Balslev coherent-wave microscopic formalism [34] is employed, within which the polarization $P_y(x)$ is expressed via the so-called coherent electron-hole interband amplitude $Y_y(\mathbf{r}, \mathbf{r})$ as follows:

$$P_y(\mathbf{r}) = 8\pi \int \mathcal{M}_y(\mathbf{r}, \mathbf{r}') Y_y(\mathbf{r}, \mathbf{r}') d^3 r'. \quad (2.13)$$

The basic equation for amplitude $Y_y(\mathbf{r}, \mathbf{r})$ within the Stahl's coherent-wave approach can be written as

$$[\mathcal{H}_{eh} - \hbar(\omega + i\nu)] Y_y(\mathbf{r}, \mathbf{r}) = \mathcal{M}_y(\mathbf{r}, \mathbf{r}') E_y(\mathbf{r}). \quad (2.14)$$

Here, $\mathbf{r} = \{x, y, z\}$ stands for the radius-vector of exciton center of mass, \mathbf{r}_r is the excitonic relative radius-vector, $\mathbf{r}_r \equiv \mathbf{r}_e - \mathbf{r}_h = \{x_r, \boldsymbol{\rho}_r\}$ with $\mathbf{r}_e = \{x_e, \boldsymbol{\rho}_e\}$ and $\mathbf{r}_h = \{x_h, \boldsymbol{\rho}_h\}$ being, respectively, the radius-vectors of electron and hole. Note that vector $\boldsymbol{\rho} = \{y, z\}$, depending on the imposed subindex, denotes the corresponding radius-vector oriented parallel to the QW plane (or the same, perpendicularly to the external dc magnetic field $\mathbf{B}_0 \parallel \mathbf{x}$). Symbol ν implies a phenomenological damping parameter. In our numerical treatment, we use the value $\hbar\nu = 1$ meV, which is typical for confined excitons in semiconductor systems (see, e.g., Refs. [30,37] and references therein).

Assuming the dc magnetic field \mathbf{B}_0 to be sufficiently strong, the Coulomb potential $U(r_r)$ of the electron-hole pair can be omitted in the two-band Hamiltonian \mathcal{H}_{eh} , which in such a case is given by

$$\mathcal{H}_{eh} = E_g + \mathcal{H}_{ex} + \mathcal{H}_{hx} + \mathcal{H}_{2D}. \quad (2.15)$$

Here, E_g represents the gap energy of the semiconductor QW material. The one-dimensional Hamiltonians \mathcal{H}_{jx} ($j = e, h$) describing the electron and hole motions along the x axis are defined by Eq. (A1) in the Appendix. The bidimensional Hamiltonian \mathcal{H}_{2D} for the electron-hole pair subjected to the static magnetic field $\mathbf{B}_0 \parallel \mathbf{x}$ is given by Eq. (A2).

Now, from the procedure described in detail at the Appendix we obtain the excitonic polarization $P_y(x)$ in the form of Eq. (A12). Afterward, substituting this $P_y(x)$ into Eq. (2.12) yields an integral equation with respect to the electric field $E_y(x)$. Remarkably, the obtained equation gets a degenerated kernel and, therefore, can be immediately resolved. The result looks like

$$\begin{aligned} E_y(x) = & \frac{ik}{k_c} \frac{\cos[k_c(d_c - x)] - I(x)}{\sin(k_c d_c)} H_z(0) \\ & - \frac{ik}{k_c} \frac{\cos(k_c x) - J(x)}{\sin(k_c d_c)} H_z(d_c); \end{aligned} \quad (2.16a)$$

$$\begin{aligned} H_z(x) = & \frac{\sin[k_c(d_c - x)] - k_c^{-1} I'(x)}{\sin(k_c d_c)} H_z(0) \\ & + \frac{\sin(k_c x) + k_c^{-1} J'(x)}{\sin(k_c d_c)} H_z(d_c). \end{aligned} \quad (2.16b)$$

Here, the prime stands for the derivative with respect to coordinate x . Also, in Eqs. (2.16), we have introduced functions $I(x)$ and $J(x)$, which are defined by Eqs. (A13) in the Appendix.

The external response of the semiconductor slab c with QW structure to an electromagnetic perturbation is intrinsically determined by the matrix $\hat{\zeta}$ of surface impedances which associates respective values of the tangential electric and magnetic fields at the left-hand ($b_L|c$), where $x = 0$, and right-hand ($c|b_R$), where $x = d_c$, interfaces of the slab:

$$\begin{pmatrix} E_y(0) \\ E_y(d_c) \end{pmatrix} = \begin{pmatrix} \zeta_{00} & -\zeta_{0d_c} \\ \zeta_{d_c0} & -\zeta_{d_cd_c} \end{pmatrix} \begin{pmatrix} H_z(0) \\ H_z(d_c) \end{pmatrix}. \quad (2.17)$$

In line with definition (2.17) and the resulting electromagnetic field distribution (2.16) mentioned before, the closed and explicit analytical expressions for the elements of surface-impedance matrix $\hat{\zeta}$ are given by

$$\zeta_{00} = \frac{ik}{k_c} \frac{\cos(k_c d_c) - I(0)}{\sin(k_c d_c)}, \quad (2.18a)$$

$$\zeta_{0d_c} = \frac{ik}{k_c} \frac{1 - J(0)}{\sin(k_c d_c)}, \quad (2.18b)$$

$$\zeta_{d_c0} = \frac{ik}{k_c} \frac{1 - I(d_c)}{\sin(k_c d_c)}, \quad (2.18c)$$

$$\zeta_{d_cd_c} = \frac{ik}{k_c} \frac{\cos(k_c d_c) - J(d_c)}{\sin(k_c d_c)}. \quad (2.18d)$$

The quantities $I(0)$, $I(d_c)$, $J(0)$, and $J(d_c)$ are particular values (A15) of functions $I(x)$ and $J(x)$ introduced by Eqs. (A13) in the Appendix. These functions are responsible for the effect of magnetoexcitonic QW on the electrodynamics of the semiconductor slab c . As the QW is absent, the functions vanish, $I(x) = 0$ and $J(x) = 0$, and all the elements of matrix $\hat{\zeta}$ degenerate into two well-known local surface impedances:

$$\zeta_{00} = \zeta_{d_cd_c} = \frac{ik}{k_c} \cot(k_c d_c), \quad (2.19a)$$

$$\zeta_{0d_c} = \zeta_{d_c0} = \frac{ik}{k_c} \frac{1}{\sin(k_c d_c)}. \quad (2.19b)$$

In the case when the QW is located asymmetrically inside the slab, see Fig. 1, the matrix elements are of different values due to different $I(0)$, $I(d_c)$, $J(0)$, and $J(d_c)$. However, when the QW is found in the middle of slab c , it turns out that $I(0) = J(d_c)$ and $I(d_c) = J(0)$. As a consequence, $\zeta_{00} = \zeta_{d_cd_c}$ and $\zeta_{0d_c} = \zeta_{d_c0}$ in the symmetric situation, and only two surface impedances remain to be independent.

III. TRANSFER RELATIONS, LOCALIZED MODES

The electromagnetic field distributions (2.3)–(2.8) and the surface impedance relation (2.17) should be complemented by continuity conditions for tangential electric and magnetic fields passing across the interfaces ($a_L|b_L$), ($b_L|c$), ($c|b_R$), and ($b_R|a_R$). As a result, we arrive at the matrix relation that determine the wave transfer throughout our setup:

$$\begin{pmatrix} A_R^+ \\ 0 \end{pmatrix} = \hat{Q} \begin{pmatrix} 1 \\ A_L^- \end{pmatrix}. \quad (3.1a)$$

The total transfer matrix \hat{Q} attaches the amplitudes, 1 and A_L^- , of incident and reflected waves in the left lead a_L to the amplitude A_R^+ of transmitted wave in the right lead a_R . It can be presented as a product of three matrices:

$$\hat{Q} = \hat{Q}^{(ba)} \hat{Q}^{(c)} \hat{Q}^{(ab)}. \quad (3.1b)$$

The matrices $\hat{Q}^{(ab)}$, $\hat{Q}^{(c)}$, and $\hat{Q}^{(ba)}$ consequentially convert the amplitudes 1 and A_L^- to amplitudes B_L^\pm , B_L^\pm to B_R^\pm , and B_R^\pm to A_R^+ and 0. Following Eqs. (2.3), (2.6) and (2.4), (2.7), the transfer matrices $\hat{Q}^{(ab)}$ and $\hat{Q}^{(ba)}$ appear to be naturally factorized into two partial transfer matrices:

$$\hat{Q}^{(ab)} = \frac{1}{2} \begin{pmatrix} e^{-\kappa_b d_b} & 0 \\ 0 & e^{\kappa_b d_b} \end{pmatrix} \begin{pmatrix} 1 + \frac{k_a}{i\kappa_b} & 1 - \frac{k_a}{i\kappa_b} \\ 1 - \frac{k_a}{i\kappa_b} & 1 + \frac{k_a}{i\kappa_b} \end{pmatrix}; \quad (3.2a)$$

$$\hat{Q}^{(ba)} = \frac{1}{2} \begin{pmatrix} 1 + \frac{i\kappa_b}{k_a} & 1 - \frac{i\kappa_b}{k_a} \\ 1 - \frac{i\kappa_b}{k_a} & 1 + \frac{i\kappa_b}{k_a} \end{pmatrix} \begin{pmatrix} e^{-\kappa_b d_b} & 0 \\ 0 & e^{\kappa_b d_b} \end{pmatrix}. \quad (3.2b)$$

In Eqs. (3.2), the diagonal matrices originate from evanescent waves (2.6) freely running inside the gap layers b_L or b_R . The other matrices are responsible for the wave pass via the interfaces ($a_L|b_L$) or ($b_R|a_R$), respectively. It is useful to note that

$$\det \hat{Q}^{(ba)} \det \hat{Q}^{(ab)} = 1 \quad \Rightarrow \quad \det \hat{Q} = \det \hat{Q}^{(c)}. \quad (3.3)$$

The matrix $\hat{Q}^{(c)}$ describes the wave transfer through the left interface ($b_L|c$), subsequent wave flight inside the semiconductor slab c interacting with magnetoexcitons of the QW, and, finally, the wave transfer through the right interface ($c|b_R$). As a consequence of Eqs. (2.6), (2.7), and (2.17), it is composed of three relevant matrices:

$$\begin{aligned} \hat{Q}^{(c)} &= \frac{1}{2} \begin{pmatrix} 1 & \frac{k}{i\kappa_b} \\ 1 & -\frac{k}{i\kappa_b} \end{pmatrix} \begin{pmatrix} \frac{\zeta_{d_cd_c}}{\zeta_{0d_c}} & \frac{\zeta_{0d_c} \zeta_{d_c0} - \zeta_{d_cd_c} \zeta_{00}}{\zeta_{0d_c}} \\ -\frac{1}{\zeta_{0d_c}} & \frac{\zeta_{00}}{\zeta_{0d_c}} \end{pmatrix} \\ &\times \begin{pmatrix} 1 & 1 \\ \frac{i\kappa_b}{k} & -\frac{i\kappa_b}{k} \end{pmatrix}. \end{aligned} \quad (3.4)$$

Solving the transfer relation (3.1a) allows us to get transmissivity $T = |A_R^+|^2$, reflectivity $R = |A_L^-|^2$, and absorption A in terms of the total transfer matrix (3.1b):

$$T = \left| \frac{\det \hat{Q}^{(c)}}{Q_{22}} \right|^2, \quad R = \left| \frac{Q_{21}}{Q_{22}} \right|^2, \quad A = 1 - R - T. \quad (3.5)$$

Determinant $\det \hat{Q}^{(c)}$ emerges in the expression for transmissivity T due to asymmetric disposition of the QW in the semiconductor slab c . When the QW is located symmetrically, i.e., in the middle of slab c (see comment at the end of Sec. II), $\det \hat{Q}^{(c)} = 1$, giving rise to the standard definition of transmissivity.

The main notion of our study is the resonant excitation of guided waves localized on the semiconductor slab c and their strong coupling with magnetoexcitons of the QW. These waves are electromagnetic eigenmodes of dielectric or conducting slabs embedded in an infinite medium. They oscillate inside the slab, however, evanescing in environment. In our setup displayed in Fig. 1, the model of semiconductor slab c containing the QW and imposed in medium b is accomplished by boundless extension of the left and right gap layers, b_L and b_R , at $d_b \rightarrow \infty$ (there are no leads a_L and a_R in this limit).

The wave transfer through such a structure is described by the transfer matrix (3.4) and looks like

$$\begin{pmatrix} B_R^+ \\ B_R^- \end{pmatrix} = \hat{Q}^{(c)} \begin{pmatrix} B_L^+ \\ B_L^- \end{pmatrix}. \quad (3.6)$$

The mode localization on slab c implies the evanescent waves (2.6) and (2.7) to contain solely the component outgoing from the slab. This requires the amplitude of incoming waves to vanish, i.e., $B_L^+ = 0$ and $B_R^- = 0$ in Eq. (3.6). In such a situation, the only nontrivial solution of Eq. (3.6) exists and equals

$$B_R^+ = Q_{12}^{(c)} B_L^- \quad \text{if and only if} \quad Q_{22}^{(c)} = 0. \quad (3.7)$$

The indispensable condition $Q_{22}^{(c)} = 0$ that relates the wave frequency ω to the wave number k_z and the other parameters of the problem serves as the dispersion equation for the electromagnetic localized modes.

With the use of explicit expression for the matrix element,

$$Q_{22}^{(c)} = \frac{\zeta_{00} + \zeta_{d_c d_c}}{2\zeta_{0d_c}} - \frac{i\kappa_b}{2k\zeta_{0d_c}} \left[\det \hat{\zeta} + \left(\frac{k}{\kappa_b} \right)^2 \right], \quad (3.8)$$

the general dispersion relation (3.7) acquires the form proper for our subsequent analysis:

$$\zeta_{00} + \zeta_{d_c d_c} = \frac{i\kappa_b}{k} \left[\det \hat{\zeta} + \left(\frac{k}{\kappa_b} \right)^2 \right]. \quad (3.9)$$

As one can readily realize, with the absent QW the degenerated surface impedances introduced by Eqs. (2.19) reduce the dispersion relation (3.9) to the conventional one:

$$\cot(k_c d_c) = \alpha_+, \quad \alpha_+ = \frac{1}{2} \left(\frac{k_c}{\kappa_b} - \frac{\kappa_b}{k_c} \right). \quad (3.10)$$

It is important to note that dispersion Eq. (3.10) permit a real-valued solution $k = k(k_z)$ solely for real-valued transverse wave number k_c of semiconductor slab c . This fact provides the basic difference between surface waves and those discussed here. Indeed, the surface modes are evanescent deep in the slab. As a result, the electromagnetic field is concentrated near both interfaces of the slab. On the contrary, our localized modes are bulk, or guided, waves. They oscillate inside the slab so the electromagnetic field is distributed over whole volume of the slab.

Figure 2 illustrates two principally distinct distributions of the electric field in the wave transferred through the entire setup of Fig. 1. The dashed green line shows typical profile of the electric field decreasing when the wave travels through the gap layers b . This causes the total reflection at the $(a_L|b_L)$ interface giving rise to exponentially small transmissivity (3.5). On the contrary, the solid red-purple line happens at the resonant transmission when the electromagnetic field in one of the gap layers b significantly increases and the localized (guided) mode is excited inside b_L - c - b_R subsystem. In the last case, the transmissivity can be substantially enhanced up to unity. What is remarkable, Fig. 2 demonstrates that the setup proposed in this paper, see Fig. 1, represents a quite efficient instrument to observe the strong photon-magnetoexciton coupling inside the optical range, provided the QW is disposed in the vicinity of great electric-field extremes inside the semiconductor QW structure.

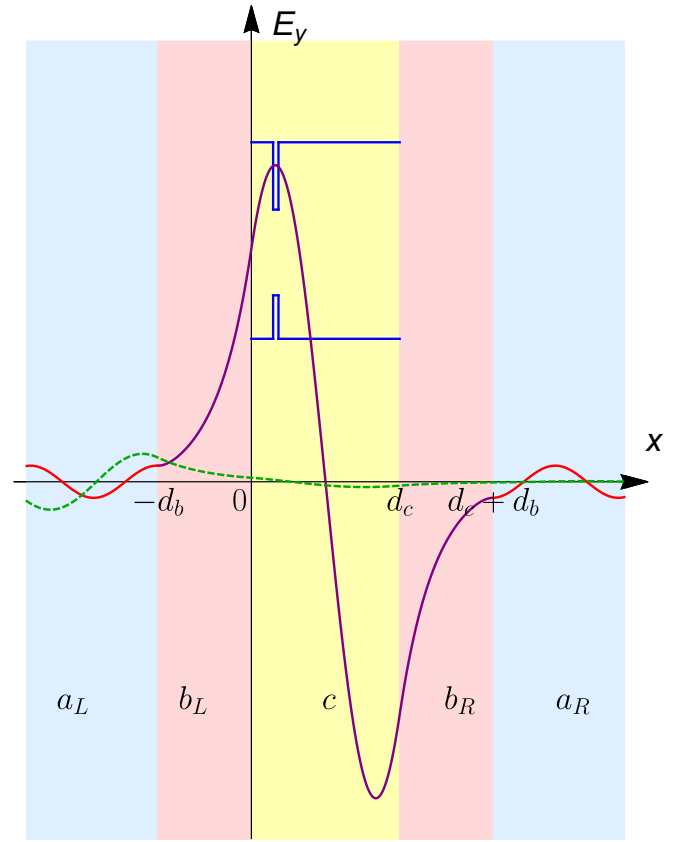


FIG. 2. The principal profiles of electric field in the wave transferred through the setup shown in Fig. 1. The solid red-purple curve exhibits the resonant wave transmission due to localized mode excited inside b_L - c - b_R subsystem and displayed by solid purple oscillating curve. The dashed green line is plotted for the typical (nonresonant) transmission when the electromagnetic flux exponentially decreases while the wave passes two gap layers, b_L and b_R .

IV. WEAKLY LOCALIZED MODE COUPLING TO MAGNETOEXCITONS

In this section, we consider the setup with two gap layers, b_L and b_R , made from ordinary dielectric with positive permittivity $\varepsilon_b > 0$. To start, we address the dispersion relation (3.10) unperturbed by the QW structure. Its real solution $k = k(k_z)$ exists only for real-valued wave number k_c , Eq. (2.11). Combining this conclusion with the appearance of κ_b to also be real, Eqs. (2.8), one can reveal that spectrum $k = k(k_z)$ of guided waves is confined to

$$k_z / \sqrt{\varepsilon_c} < k < k_z / \sqrt{\varepsilon_b} \quad \Rightarrow \quad \varepsilon_b < \varepsilon_c. \quad (4.1)$$

Within interval (4.1), the localized modes oscillate inside slab c and attenuate in the left b_L and right b_R gap layers moving away from the slab over the relatively great scale κ_b^{-1} . Therefore, we call guided waves localized on slab surrounded by an optically softer medium with lower permittivity ($\varepsilon_b < \varepsilon_c$) *weakly localized modes*.

The dispersion relation (3.10) can be rewritten in another suitable form,

$$k_c d_c = \pi p + \text{arccot } \alpha_+, \quad p = 0, 1, 2, 3, \dots, \quad (4.2)$$

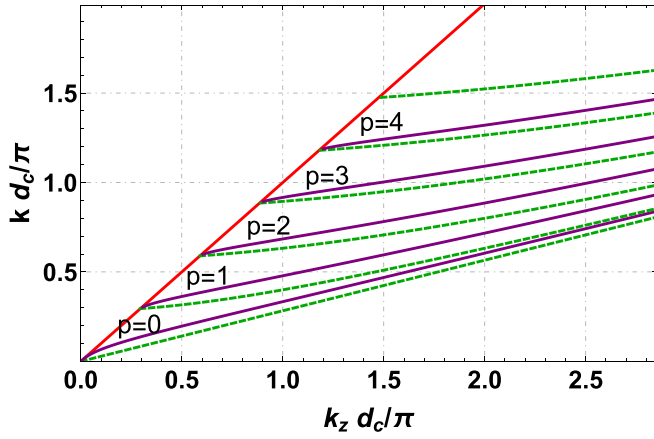


FIG. 3. Solid purple spectral curves $k = k_p(k_z)$ of localized (guided) modes obeying dispersion relation (4.2) with $p = 0, 1, 2, 3, 4$. The red light line corresponds to the right restricting condition (4.1). The dashed green curves $k = k_p^r(k_z)$ demonstrate the borders of the existence domain (4.3) of $k = k_p(k_z)$. Permittivities used here: $\varepsilon_b = 1$ (air), $\varepsilon_c = 12.5$.

from which the localized mode spectrum $k = k(k_z)$ follows to consist of an infinite set (family) of p th dispersion curves $k = k_p(k_z)$ enumerated by index p and shown in Fig. 3.

In accordance with confinement (4.1), all the dispersion curves $k = k_p(k_z)$ are arranged within a domain between two light lines, $k = k_z/\sqrt{\varepsilon_c}$ and $k = k_z/\sqrt{\varepsilon_b}$. Then, since by definition $0 \leq \arccot \alpha_+ \leq \pi$, every p th spectral curve $k = k_p(k_z)$ is found in its own domain specified by

$$k_p^r(k_z) < k_p(k_z) < k_{p+1}^r(k_z),$$

$$\text{with } k_p^r(k_z) = \sqrt{(\pi p/d_c)^2 + k_z^2/\varepsilon_c}. \quad (4.3)$$

Note that the lowest border $k = k_0^r(k_z)$ coincides with the light line $k = k_z/\sqrt{\varepsilon_c}$ from the left restricting condition of Eq. (4.1).

The spectrum $k = k_0(k_z)$ of the lowest guided zero mode starts at the coordinate origin ($k_z = 0, k = 0$) and, with increasing k_z , monotonically increases along the light line $k = k_z/\sqrt{\varepsilon_b}$. Afterward, obeying asymptotics

$$k \approx \frac{k_z}{\sqrt{\varepsilon_b}} \left[1 - \frac{(\varepsilon_c - \varepsilon_b)^2}{8\varepsilon_b^2} (k_z d_c)^2 \right] \quad \text{for } (k_z d_c)^2 \ll 1, \quad (4.4)$$

it is deflected down and at $k_z d_c \gg 1$ approaches from below its upper border $k = k_1^r(k_z)$, Eq. (4.3).

The dispersion curves $k = k_p(k_z)$ supporting each of nonzero modes ($p \neq 0$) start from the threshold

$$k_z = k_z^{cr} \equiv \frac{\pi p}{d_c} \sqrt{\frac{\varepsilon_b}{\varepsilon_c - \varepsilon_b}}, \quad k = k_p^{cr} \equiv k_z^{cr}/\sqrt{\varepsilon_b}, \quad (4.5)$$

which is a crossing point of the upper light line $k = k_z/\sqrt{\varepsilon_b}$ and the lower (left) border $k = k_p^r(k_z)$ depicted, respectively, by red line and dashed green curves in Fig. 3. After the threshold, the behavior of the p th spectral curve $k = k_{p \neq 0}(k_z)$

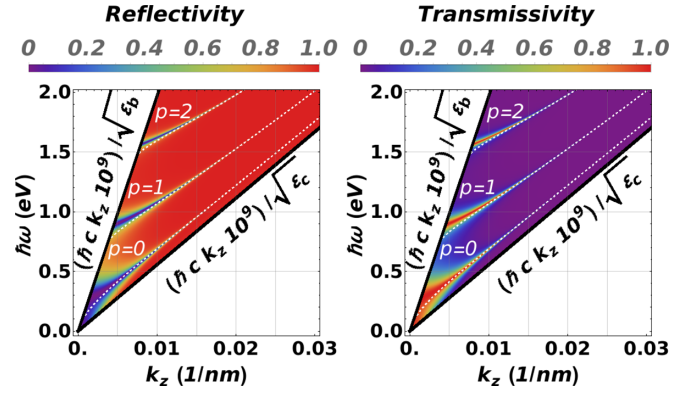


FIG. 4. Reflectivity R and transmissivity T , Eqs. (3.5), versus wave number k_z and frequency $\hbar\omega$. The dashed white lines display the dispersion curves of $\hbar\omega$ versus k_z for the localized modes, Eq. (4.2) and Fig. 3. Parameters used here: $\varepsilon_a(\omega)$ (Si) as a function of ω is varied from 12 to 15, $\varepsilon_b = 1$ (air), $\varepsilon_c = 12.5$, $d_b = 157$ nm and $d_c = 250$ nm.

is described by approximation:

$$k - k_p^{cr} \approx \frac{2}{\pi p} \sqrt{\frac{k_z^2 - k_z^{cr2}}{\varepsilon_c - \varepsilon_b}} \ll 1. \quad (4.6)$$

Sufficiently far from the threshold, the spectrum $k = k_p(k_z)$ closes to its upper (right) border, see Eqs. (4.3):

$$k \approx k_{p+1}^r(k_z) \quad \text{for } k_z \gg k_z^{cr}. \quad (4.7)$$

Remarkably, following Eqs. (4.1) and (4.3), as $k_z \rightarrow \infty$, all the dispersion curves $k = k_p(k_z)$ of the electromagnetic p modes localized on the semiconductor slab c , as well as their borders $k_p^r(k_z)$, get thick to the lowest confining light line $k = k_z/\sqrt{\varepsilon_c}$, Eq. (4.1). However, in this tendency, the hierarchy of modes and borders still remains: the greater the index p , the higher the corresponding guided mode.

Now let us proceed focusing our study on resonant excitation of weakly localized modes and their coupling to magnetoexcitons of the QW structure. In the configuration of our setup, Fig. 1, such an excitation is possible if the dielectric leads, a_L and a_R , are optically denser than the dielectric gap layers, b_L and b_R :

$$0 < \varepsilon_b < \varepsilon_a. \quad (4.8)$$

Indeed, this assumption provides the wave number k_b defined by Eq. (2.8) to be imaginary even under the constitutive restriction (2.2) due to which the wave number k_a , Eq. (2.5), of incident, reflected, and transmitted waves is real.

Note, in an experiment, the air with $\varepsilon_b = 1$ is relevant to serve as a filling material for the gap layers b . Despite this circumstance, we keep the notation ε_b to extend applicability of our results.

Figure 4 illustrates unperturbed by the QW optical spectra of reflectivity R and transmissivity T on the (k_z, ω) plane within the colored region corresponding to confinement (4.1). Here and in the further analysis, the prisms a_L and a_R are assumed to be made from Si, taking into account not only the dispersion of Si permittivity $\varepsilon_a(\omega)$ but also the fact that energy losses in Si, within the interval from zero to 2 eV,

are negligible. In the frequency ranges [0.06,0.6] eV and [1,2] eV, the data for $\varepsilon_a(\omega)$ were taken from Refs. [39,40], correspondingly. The data for narrow initial and intermediate intervals, [0,0.06] eV and [0.6,1] eV, were obtained by extrapolating the data from Refs. [39] and [40]. Thus, due to frequency dispersion, $12 \leq \varepsilon_a(\omega) \leq 15$ within the whole frequency range considered in our paper. Due to selected values of $\varepsilon_b < \varepsilon_c \lesssim \varepsilon_a$, the determinative restrictions (2.2) and (4.8) are fulfilled automatically. In both panels, the red color corresponds to the greater values (up to one), whereas the dark blue color marks the smaller values (up to zero) of R and T . In addition, the dispersion curves $\omega = \omega_p(k_z)$ of the localized modes, which are equivalent to $k = k_p(k_z)$ with $k = \omega/c$, are plotted in the dashed white. As expected, the narrow regions where the reflection almost vanishes ($R \approx 0$), while the transmission happens to be perfect ($T \approx 1$), closely trace the relevant dashed-white dispersion curves. The visible deviations at small k_z are related to the fact that our setup includes the connecting leads, a_L and a_R , resulting in a finite value of thickness d_b of the gap layers, b_L and b_R . While the conventional dispersion relation (3.7) is obtained for semi-infinite b gaps, in a real setup their thickness d_b slightly alter it, see Ref. [31]. Thus, Fig. 4 elucidates the perfect transmission with $T = 1$ and $R = 0$ emerging due to excitation of the electromagnetic modes localized on the semiconductor slab c .

Figure 5 depicts the reflectivity R , transmissivity T , and absorption A spectra, depending on the wave vector component k_z and frequency ω for the nonlocal setup including a GaAs QW embedded in the semiconductor slab c ($\text{In}_{0.18}\text{Ga}_{0.82}\text{As}|\text{GaAs}|\text{In}_{0.18}\text{Ga}_{0.82}\text{As}$), which is sandwiched between two Si dielectric leads, a_L and a_R , and separated from them by two air gap layers, b_L and b_R (see Fig. 1). The air gap layers b are characterized by permittivity $\varepsilon_b = 1$ and thickness $d_b = 157$ nm. The left QW interface ($\text{In}_{0.18}\text{Ga}_{0.82}\text{As}|\text{GaAs}$) is placed at coordinate $x_1 = 42$ nm corresponding to the antinode of the electric field for the localized mode. The coordinate of the right QW interface ($\text{GaAs}|\text{In}_{0.18}\text{Ga}_{0.82}\text{As}$) is $x_2 = 47$ nm. The total thickness of slab c is $d_c = 250$ nm. All the other QW parameters are taken from Refs. [30,37]. In the calculations of the presented spectra, the electron-hole Coulomb interaction has been neglected, since the value of external dc magnetic field, applied to the setup, is taken to be sufficiently great, $B_0 = 30$ T (see Sec. VI). In addition, the dashed white lines in Fig. 5 trace the dispersion curve $k = k_p(k_z)$ with $p = 1$ of the waveguide mode for a slab c without the QW, see Eq. (4.2) and Fig. 3. The spectra are plotted near eigenenergies (black dotted lines) of the $e1 - hh1$ magnetoexciton states (n, m) , where integers n and m enumerate, respectively, the Landau levels and angular momentum of magnetoexciton (see the Appendix). One can clearly observe the anticrossings of the waveguide spectral curves with the magnetoexciton levels, which are characteristic of the strong-coupling regime. Indeed, as seen in Fig. 5, the strong coupling is remarkable for the localized mode with $p = 1$ coupled to the magnetoexcitons of levels $(n, m) = (0, 0)$ and $(n, m) = (1, 0)$, since a noticeable Rabi splitting arises.

Figure 6 displays the reflection spectra for the semiconductor heterostructure as in Fig. 5, calculated at different

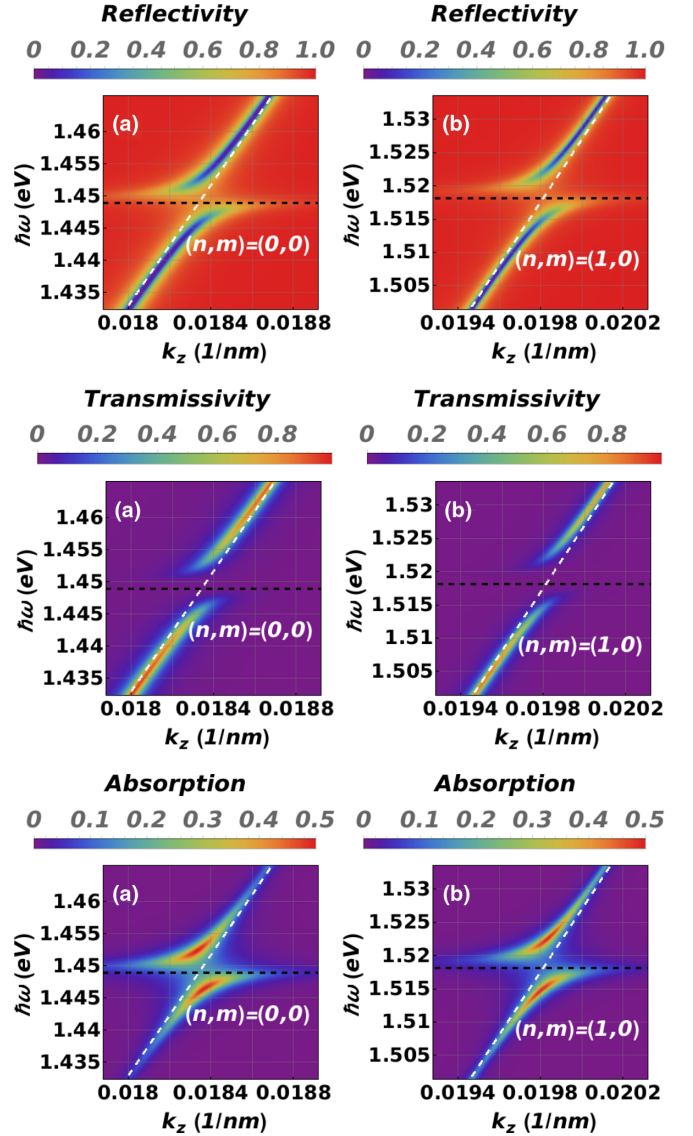


FIG. 5. Reflectivity R , transmissivity T , and absorption A , Eqs. (3.5), versus k_z and $\hbar\omega$ for GaAs QW embedded in $\text{In}_{0.18}\text{Ga}_{0.82}\text{As}$ semiconductor slab which is sandwiched between two Si dielectric leads and separated from them by two air gap layers near the eigenenergies of magnetoexciton states with $(n, m) = (0, 0)$ (left panels) and $(n, m) = (1, 0)$ (right panels) and slab localized modes with $p = 1$. The applied magnetic field everywhere throughout the paper is of magnitude $B_0 = 30$ T.

incidence angles $\theta = \arcsin(k_z/k\sqrt{\varepsilon_a})$. At $\theta = 42.9^\circ$ (blue line), a prominent dip corresponding to the excitation of the $p = 1$ electromagnetic localized mode is observed, whereas the magnetoexciton states with $(n, m) = (0, 0)$ and $(n, m) = (1, 0)$ are optically manifested as small dips. At a greater incidence angle, specifically, at $\theta = 43.2^\circ$ (purple line), the spectral curve $k = k_1(k_z)$ of the waveguide mode happens to be found near the eigenenergy of the magnetoexciton $(n, m) = (0, 0)$. As a result, we see two huge dips whose separation (Rabi splitting) is around 12 meV. For $\theta = 43.9^\circ$ (red line), the mode spectrum $k = k_1(k_z)$ is shifted to higher energies and, consequently, the effect of the magnetoexciton level

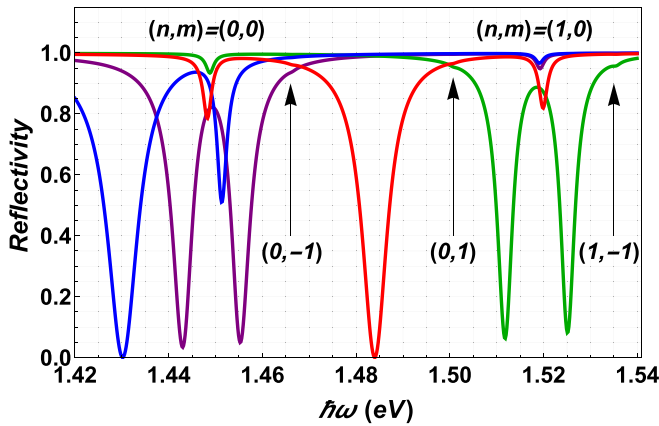


FIG. 6. Reflectivity R versus frequency $\hbar\omega$ for the same semiconductor heterostructure as in Fig. 5 at several values of incidence angle θ . Blue, purple, red, and green lines correspond to $\theta = 42.9^\circ$, $\theta = 43.2^\circ$, $\theta = 43.9^\circ$, and $\theta = 44.5^\circ$, respectively.

$(n, m) = (0, 0)$ becomes weak. Reaching the angle $\theta = 44.5^\circ$ (green line), the strong coupling of the localized mode with another magnetoexciton level $(n, m) = (1, 0)$ gives rise to the appearance of two huge dips with Rabi splitting being about 13 meV.

It is interesting that in Fig. 6 we can also observe reflectivity features associated with the excitation of magnetoexciton states (n, m) with nonzero angular momentum m , specifically, $(0, -1)$, $(0, 1)$, and $(1, -1)$. However, their optical manifestation is quite weak. Indeed, according to our analytical results, Eqs. (A9) and (A12), the ratio between the oscillator strengths for magnetoexcitons with $m \neq 0$ and for those with $m = 0$ is of the order of $|G_{n,m \neq 0}(k_z r_B)|^2 / |G_{n,0}(k_z r_B)|^2 \ll 1$ as $(k_z r_B)^2 \ll 1$. The reason for the coupling between photons and magnetoexcitons with nonzero azimuthal quantum number, $m \neq 0$, emerges due to the breaking of the axial symmetry by the tangential component of wave vector k_z . This effect is similar to that produced by a dc electric field parallel to the slab plane (see details in Refs. [30,37]).

V. STRONGLY LOCALIZED MODE COUPLING TO MAGNETOEXCITONS

To proceed further, let us recall that through the entire investigation we consider the electromagnetic waves of TE polarization (or the same of s polarization) with configuration given by Eqs. (2.1).

The other way to achieve the resonant excitation of the guided waves localized on the semiconductor slab c is to construct the gap layers, b_L and b_R , from material with negative dielectric permittivity $\varepsilon_b < 0$. In such a case, wave number k_b is imaginary by definition (2.8), giving rise to evanescent waves inside the gap layers b . As a consequence, the existence domain of the real-valued solution $k = k(k_z)$ of the unperturbed by the QW dispersion relation (3.10) contains just restriction from below,

$$k_z / \sqrt{\varepsilon_c} < k, \quad (5.1)$$

that provides wave number k_c in the semiconductor slab c , Eq. (2.11), to also be real valued.

A quite typical and simple in realization example is represented by a pure metal, whose permittivity $\varepsilon_b < 0$ given by the Drude model, within the underplasma frequency ω_p range, reads

$$\varepsilon_b = -\omega_p^2 / \omega^2 = -(k\delta)^{-2}, \quad \delta = c / \omega_p$$

when $\omega \ll \omega_p \Leftrightarrow k\delta \ll 1$. (5.2)

Here, δ serves as the minimal skin depth of electromagnetic field penetration in a bulk metal. In the model (5.2), the decrement of guided wave attenuation κ_b from Eq. (2.8) looks like

$$\kappa_b = \sqrt{k_z^2 + \delta^{-2}} \quad (5.3)$$

and does not depend on the total wave number $k = \omega/c$. Due to the extremely small value of $\delta \sim 10 - 100$ nm, we call guided waves localized on slab surrounded by metal *strongly localized modes*.

The dispersion relation (3.10) is proper to rewrite as

$$k_c d_c = \pi s - (\pi - \text{arccot } \alpha_+), \quad s = 1, 2, 3, \dots \quad (5.4)$$

The guided mode spectrum $k = k(k_z)$, governed by Eq. (5.4), contains an infinite set (family) of s th dispersion curves $k = k_s(k_z)$ enumerated by index s . Here, we have accepted a mode classification traditional for waveguides with ideally specular boundaries, where the lowest mode gets index $s = 1$. The evident relation between indices s and p from the dispersion Eq. (4.2) is $s = p + 1$.

Since the absolute value of ε_b is extremely great, it is reasonable to assume the background permittivity ε_c of the semiconductor slab c to be relatively small:

$$0 < \varepsilon_c \ll |\varepsilon_b| \Leftrightarrow k\delta\sqrt{\varepsilon_c} \ll 1. \quad (5.5)$$

Such an assumption makes evident $k_c / \kappa_b \ll 1$ and $\alpha_+ \approx -\kappa_b / 2k_c$. This allows us to change $\text{arccot } \alpha_+$ to its approximation $\text{arccot } \alpha_+ \approx \pi - 2k_c / \kappa_b$ in the dispersion relation (5.4). As a result, we realize the desired family of spectral curves $k = k_s(k_z)$ being described by

$$k_s(k_z) = \sqrt{\left(\frac{\pi s}{d_c}\right)^2 \left(1 + \frac{2}{\kappa_b d_c}\right)^{-2} + k_z^2} / \sqrt{\varepsilon_c}. \quad (5.6)$$

As could be expected, Eq. (5.6) slightly differs from the spectrum of a planar waveguide with perfectly conducting plane boundaries. The small correction is caused by the finite-valued high-frequency conductivity of a metal taken into account in our model.

Figure 7 exhibits spectrum $k = k_s(k_z)$ calculated numerically from the dispersion relation (5.4) in the solid purple and from asymptotical Eq. (5.6) in the dashed green. As one can see, due to extremely great plasma frequency ω_p of conduction electrons leading to extremely small electromagnetic skin depth δ , the distinction between two kinds of the curves is practically invisible in the scale of the figure. Every spectral curve $k = k_s(k_z)$ of the guided modes starts from the threshold at $k_z = 0$ and monotonically increases with k_z following Eq. (5.6). All the spectral curves run above the light line $k = k_z / \sqrt{\varepsilon_c}$, according to obligatory condition (5.1).

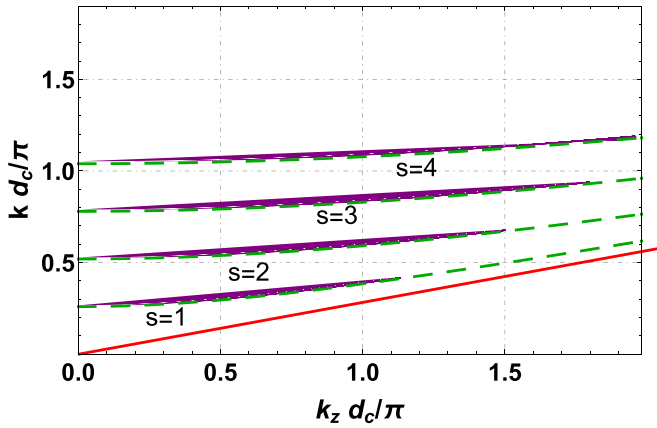


FIG. 7. Spectrum $k = k_s(k_z)$ of guided modes versus k_z governed by dispersion relation (5.4) (solid purple curves) and obeying asymptotics (5.6) (dashed green curves) for the semiconductor slab c surrounded by metal medium. The red light line is $k = k_z / \sqrt{\epsilon_c}$ from Eq. (5.1). Parameters: $\omega_p = 15$ eV (Al), $\epsilon_c = 12.5$.

Our numerics of the reflection and transmission spectra, R and T , based on exact Eqs. (3.5), for the unperturbed by the QW setup constructed from Si leads a and Al gap layers b are drawn in Fig. 8. The characteristic parameters are given in the figure caption. For the metal permittivity, we employ the Drude model, in which the displacement current and the electron relaxation rate ν_{met} is taken into account for more accuracy:

$$\epsilon_b(\omega) = 1 - \frac{\omega_p^2}{\omega(\omega + i\nu_{\text{met}})}. \quad (5.7)$$

Nevertheless, we have neglected the magneto-optical effect in Eq. (5.7) considering that in comparison with the applied range of high wave-frequency ω , the cyclotron frequency $\Omega = eB_0/m^*c$ of the external dc magnetic field B_0 is relatively small, $\Omega^2 \ll |\omega + i\nu_{\text{met}}|^2$, where m^* is the effective electron mass. To identify the origin of the perfect transmission and null reflection, we also place the relevant dispersion curves $\omega = \omega_s(k_z)$ of the guided modes calculated from Eq. (5.4) and

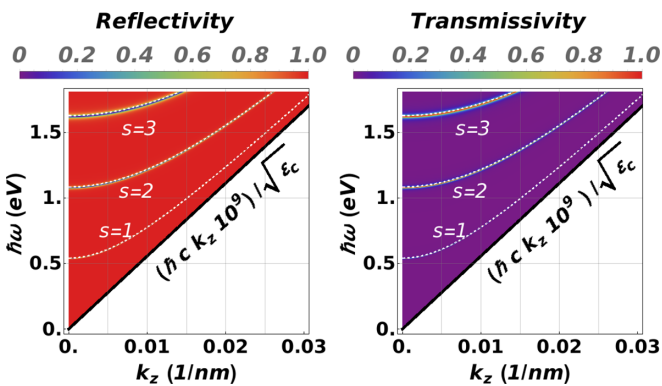


FIG. 8. Reflectivity R and transmissivity T , Eqs. (3.5), versus wave number k_z and frequency $\hbar\omega$ of the unperturbed setup with metal gap layers b . The dashed white lines represent the dispersion curves $k = k_s(k_z)$ of localized modes. Parameters: $\epsilon_a(\omega)$ (Si) is the same permittivity mentioned in Fig. 4; $\omega_p = 15$ eV, $\nu_{\text{met}} = 5.55 \cdot 10^{-3} \omega_p$ (Al); $d_b = 20$ nm, $\epsilon_c = 12.5$, $d_c = 296$ nm.

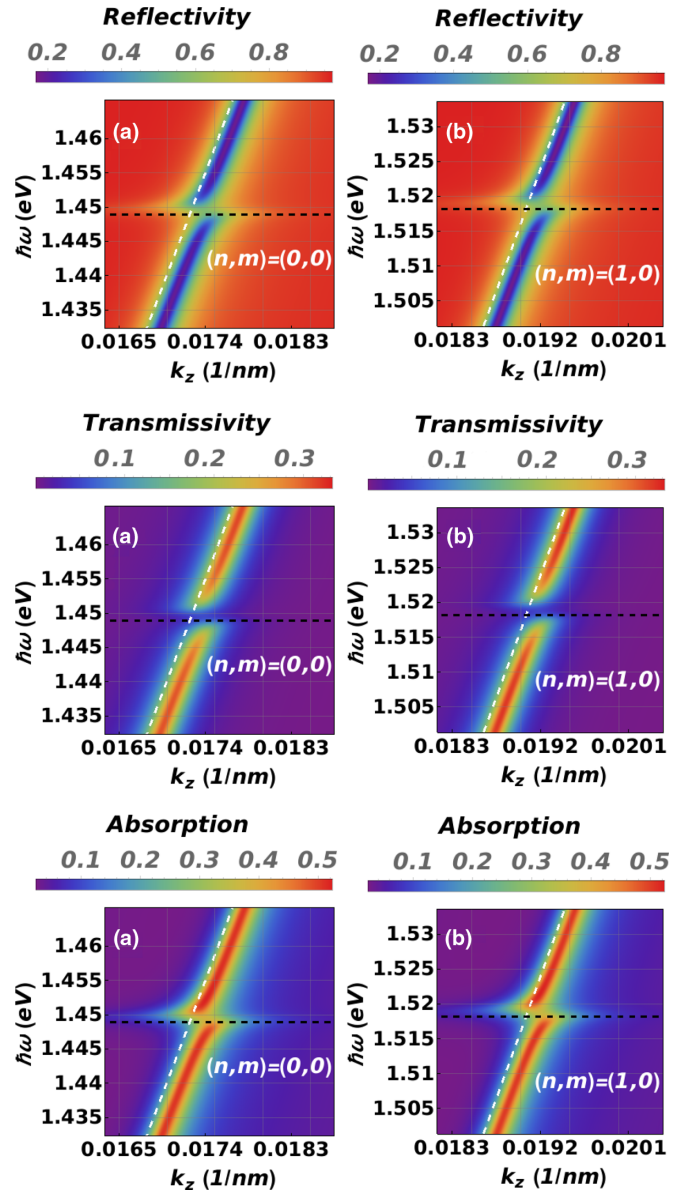


FIG. 9. Reflectivity R , transmissivity T , and absorption A , Eqs. (3.5), versus k_z and $\hbar\omega$ for GaAs QW embedded in $\text{In}_{0.18}\text{Ga}_{0.82}\text{As}$ semiconductor slab which is surrounded by two Si dielectric leads and separated from them by two Al layers, near the eigenenergies of magnetoexciton states with $(n, m) = (0, 0)$ (left panels) and $(n, m) = (1, 0)$ (right panels) and guided modes with $s = 2$. The magnitude of the applied magnetic field everywhere is $B_0 = 30$ T.

shown by the dashed white lines. Even a passing glance on Fig. 8 ensures that the perfect transmission with $T = 1$ and $R = 0$ arises as a consequence of the resonant excitation of the electromagnetic modes localized on the semiconductor slab c sandwiched between the metal gap layers b , which are, respectively, connected to the light emitter and receiver (leads a).

Figure 9 illustrates reflectivity R , transmissivity T , and absorption A spectra as functions of the wave number k_z and frequency ω for the setup including metallic (Al) microcavity with a slab c composed of two $\text{In}_{0.18}\text{Ga}_{0.82}\text{As}$ barriers and a GaAs QW. The left QW boundary is placed at the position

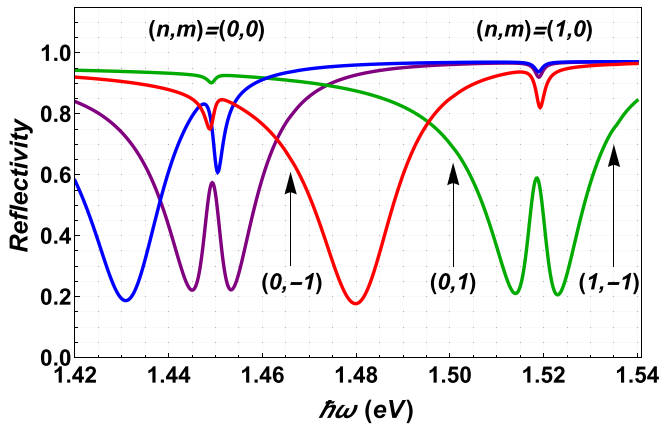


FIG. 10. Reflectivity R versus frequency $\hbar\omega$ (eV) for the QW structure c surrounded by metal (Al) gap layers b at the incidence angles $\theta = 39.8^\circ$ (blue line), $\theta = 40.4^\circ$ (purple line), $\theta = 41.5^\circ$ (red line), and $\theta = 42.7^\circ$ (green line).

of antinode of the electric component for the localized mode, which is $x_1 = d_c/3$. The QW width is $x_2 - x_1 = 5$ nm. The other parameters are provided in the caption to Fig. 8. The whole metallic microcavity is embedded in a Si medium (the leads a in Fig. 1). As in the previous section, our numerical results correspond to the case when the Coulomb interaction between the electron-hole pair is negligible. The optical spectra were calculated near the magnetoexciton resonances $(n, m) = (0, 0)$ and $(n, m) = (1, 0)$ (black dotted lines). The dashed white line traces the dispersion curve $k = k_s(k_z)$, Eq. (5.4), of the localized mode with index $s = 2$ also drawn in Fig. 8. In Fig. 9, we can clearly see significant anticrossings (Rabi splitting) of the spectral curves of localized mode and magnetoexciton levels, which are attributed to the strong-coupling regime.

Figure 10 shows the reflection spectra of the metallic (Al) microcavity with an embedded GaAs QW mentioned above, which were calculated for several incidence angles $\theta = \arcsin(k_z/k\sqrt{\epsilon_a})$, under the same conditions as in Fig. 9. At $\theta = 39.8^\circ$ (blue line), a huge dip associated with excitation of guided mode is revealed while the magnetoexciton levels with $(n, m) = (0, 0)$ and $(n, m) = (1, 0)$ produce very small dips. At $\theta = 40.4^\circ$ (purple line), the spectrum $k = k_2(k_z)$, Eq. (5.4), of localized mode coincides with magnetoexciton state $(n, m) = (0, 0)$. As a result of strong coupling, the common dip increases and splits into two bright ones. Here, we see that the Rabi splitting is around 9 meV. For $\theta = 41.5^\circ$ (red line), the localized-mode dip has been shifted to an energy higher than that of the magnetoexciton $(n, m) = (0, 0)$. As a consequence, the magnetoexciton $(n, m) = (0, 0)$ feature turns into a small single dip. At an incidence angle θ as large as 42.7° (green line), the resonance between the electromagnetic guided mode of $s = 2$ and the magnetoexciton $(n, m) = (1, 0)$ emerges. Therefore, the corresponding enormous dip splits into two bright dips with the Rabi splitting being around 9 meV. In addition, the reflectivity spectra shown in Fig. 10 manifests the very weak and practically imperceptible coupling between the localized wave mode and the magnetoexcitons with nonzero azimuthal quantum number ($m \neq 0$).

VI. DISCUSSION

The model and results presented above neglect the Coulomb interaction between the electron and hole. Such a limiting case in semiconductor QW heterostructures is good enough to obtain physical insight of the studied phenomena with mathematical transparency (see, for example, Refs. [30,37,41]). In our paper, this approximation allowed us to derive closed and explicit analytical expressions for the elements of the surface-impedance matrix $\hat{\zeta}$, Eqs. (2.18), providing a deep understanding of the coupling between either weakly or strongly localized modes and magnetoexcitons. The approximation is valid when the magnetoexciton cyclotron energy $\hbar\omega_c$ is much larger than the binding energy E_b associated with the Coulomb interaction. However, for typical values of the magnetic field applied in experiments, which are lower than a few tens of Teslas, the cyclotron and binding energies turn out to be comparable. For this reason, it is necessary to carry out numerical calculations. As established in Refs. [30,37], the main effect of the Coulomb interaction is a redshift of the magnetoexciton low-energy levels. Our numerics performed for the here-considered setup, being compared with the presented analytical predictions, confirm the above conclusion. Indeed, for $B_0 = 30$ T, and a GaAs QW width $x_2 - x_1 = 5$ nm, $\hbar\omega_c \approx 69$ meV, $E_b \approx 19$ meV [42], the redshift is ≈ 15 meV. Being comparable with the binding energy E_b , the shift, however, turns out to be about five times smaller than the cyclotron energy $\hbar\omega_c$. As a consequence, the incidence angle θ range inside which the strong coupling between the localized mode and magnetoexciton occurs, is slightly shifted to lower values.

The results presented in our paper elucidate that generation of electromagnetic localized (guided) modes, strongly coupled to magnetoexcitons of a semiconductor slab with a QW, can be accomplished with the use of the optical technique based on the phenomenon of *breaking* of the TIR. Such a phenomenon can result either from the resonantly enhanced transmission (called *frustrated* TIR) in the case of unilateral wave excitation [33,43–45] or from a resonant increase of the light absorption (called *attenuated* TIR) at both unilateral [33] and bilateral [31,32] wave excitations of an experimental setup. For a metal microcavity (the setup with metallic gap layers), the results might look unsurprising because the excitation and strong coupling of those modes has been observed in Refs. [17–21] as well as in Refs. [29,30] for the well-known semiconductor quantum microcavities. However, the results presented in our paper for a semiconductor slab covered by dielectric (air) gap layers turn out to be rather unexpected, since in such a heterostructure the electromagnetic modes are weakly localized and their coupling to magnetoexcitons confined to a QW is believed to be also weak [37]. Despite this opinion, the here-calculated (k_z, ω) spectra of reflection, transmission, and absorption show that the resonant excitation of weakly guided modes can be accompanied by their strong coupling with magnetoexcitons of a QW. Moreover, the energy splitting (≈ 13 meV, see Sec. IV) in the setup composed of a semiconductor slab embedded in air, is greater than those in the cases of semiconductor [30] and metal microcavities (≈ 9 meV, see Sec. V). It should be commented that the predicted coupling between magnetoexciton and guided

modes has been classified as strong because of the appearance of Rabi splitting. In the case of magnetoexcitons, the appearance of very strong coupling requires the Rabi splitting to be comparable with the magnetoexciton cyclotron energy. In our paper, the Rabi splitting is 9 – 13 meV whereas the magnetoexciton cyclotron energy is 69 meV at $B_0 = 30$ T.

It is important to emphasize that our analytical results and numerics reveal the notable sensitivity of the coupling strength to the QW location with respect to the distribution of a guided mode field inside the semiconductor. Due to this, for any given mode the strong coupling can be achieved by proper tuning of the QW position. Considering that there is no energy losses in air, unlike metal, the air gap layers b can have larger thickness that provide the localized modes to be more pronounced. At the same time, the metal layer thickness d_b should not be much larger than the corresponding electromagnetic skin depth δ to observe the resonant transmission. From the experimental point of view, the latter is an advantage of using air gap layers. In addition, the air gap layers b can also be substituted by a low-refractive-index dielectric provided conditions $\varepsilon_b < \varepsilon_a$ and $\varepsilon_b < \varepsilon_c$ are fulfilled to guarantee the excitation of localized modes with *breaking* the TIR.

VII. CONCLUSIONS

We have analyzed the excitation of electromagnetic modes localized on a semiconductor guiding slab and being strongly coupled with magnetoexcitons of a QW included in the slab. To this end, we consider the setup arranged for the application of an optical technique based on the breaking of the TIR that requires the use of two external leads (or prisms) and two gap layers covering the semiconductor waveguide.

In the case of metallic gap layers, the setup can be regarded as the so-called metal microcavity (a metal involves QW structure that serves as a microcavity). Here, the electromagnetic modes occur to be strongly localized. The calculated spectra exhibit a resonant structure associated with the excitation of the localized modes and their strong coupling with confined magnetoexcitons. On the other hand, in a semiconductor slab sandwiched between dielectric (air) gap layers, the guided modes turn out to be weakly localized. Notwithstanding, the resonant excitation of guided modes and their strong coupling to confined magnetoexcitons is attained. It is noteworthy that the Rabi splitting is greater for a semiconductor slab covered by a dielectric (air) in comparison with that observed in metal and semiconductor microcavities. Employing gap layers of air or low-refractive-index dielectrics together with two external leads/prisms can be useful in designing low losses and simpler optical devices.

Our results are verified by comparing the unperturbed by coupling dispersion curves of localized modes obtained analytically and the numerically calculated resonant optical spectra of reflectivity, transmissivity, and absorption.

There exists a common belief that almost all fundamental electrodynamic phenomena, especially within terahertz and optical frequency range, manifest themselves mostly in the TM polarization. The classical examples are surface waves in nonmagnetic media and plasmons. In our paper, we choose the TE polarization to claim that it can also support interesting and significant optical effects. Undoubtedly, the resonant

excitation of guided waves localized on semiconductor QW structures and their strong coupling with magnetoexcitons must be observed in TM polarization as well. However, analytical treatment of the magnetoexciton-photon interaction turns out to be more straightforward in the TE polarization due to existence of the only component of electric field. In addition, as known, surface waves do not exist in TE polarization, while localized waves are allowed. Therefore, it seems to us that in the TE polarization, the effects analyzed in our paper can be realized more apparently without accompaniment of other effects. Thus, the TE polarization may be more suited for experiments.

ACKNOWLEDGMENTS

This work was supported by BUAP (MX).

APPENDIX: ON ELECTROMAGNETIC FIELD DISTRIBUTION IN SEMICONDUCTOR SLAB WITH QUANTUM WELL

Here, we reveal more details in deriving Eqs. (2.16) for the electromagnetic field in slab c including the QW.

We start from explanation of the structure of the two-band Hamiltonian \mathcal{H}_{eh} entering the basic Eq. (2.14). In Eq. (2.15), the one-dimensional Hamiltonians \mathcal{H}_{jx} ($j = e, h$) are responsible for the quantization of the electron/hole motion along the x axis (see Fig. 1),

$$\mathcal{H}_{jx} = -\frac{\hbar^2}{2m_{jx}} \frac{\partial^2}{\partial x_j^2} + V_j(x_j), \quad j = e, h, \quad (\text{A1})$$

with m_{jx} and $V_j(x_j)$ being, respectively, the effective mass and the steplike confining potential. Specifically, $V_j(x_j) = 0$ inside the QW where $x_1 < x_j < x_2$ and $V_j(x_j) = V_0^j > 0$ otherwise.

The bidimensional Hamiltonian \mathcal{H}_{2D} in Eq. (2.15) for the electron and hole under the quantizing action of the dc magnetic field $\mathbf{B}_0 \parallel \mathbf{x}$, has the form

$$\mathcal{H}_{2D} = \frac{1}{2m_{e\parallel}} \left(i\hbar \nabla_{\rho_e} - \frac{e}{c} \mathbf{A}_e \right)^2 + \frac{1}{2m_{h\parallel}} \left(i\hbar \nabla_{\rho_h} + \frac{e}{c} \mathbf{A}_h \right)^2, \quad (\text{A2})$$

where the elementary charge is denoted as $e > 0$, and $m_{j\parallel}$ ($j = e, h$) implies the electron/hole effective mass in perpendicular to \mathbf{B}_0 direction (parallel to the QW plane). In Eqs. (A1) and (A2), it was assumed that the effective masses ($m_{jx}, m_{j\parallel}$) are constants in the entire semiconductor slab c ($0 \leq x \leq d_c$). The vector potential \mathbf{A}_j of the dc magnetic field $\mathbf{B}_0 = \{B_0, 0, 0\}$ is chosen in the following calibration:

$$\mathbf{A}_j = \frac{1}{2} \mathbf{B}_0 \times \boldsymbol{\rho}_j, \quad j = e, h. \quad (\text{A3})$$

The quantity $\mathcal{M}_y(\mathbf{r}_r)$ that appears in Eqs. (2.13) and (2.14) indicates the interband-transition dipole density, which is taken within the so-called shell model [46]. Specifically,

$$\mathcal{M}_y(\mathbf{r}_r) = \frac{M_0}{2\pi \rho_r} \delta(x_r) \delta(\rho_r - 0), \quad (\text{A4})$$

where factor M_0 is called the integrated dipole transition matrix, $\delta(\dots)$ implies the Dirac delta-function.

In line with the procedure proposed in Ref. [37], the solution of the problem consisting of Eqs. (2.13) and (2.14) is found as an expansion in the eigenfunctions of magnetoexcitonic Hamiltonian H_{eh} , Eq. (2.15), with the use of Eqs. (A1)–(A4). After explicitly deriving the emerging integrals and a little bit cumbersome algebra, we arrive at the nonlocal relation between the excitonic polarization $P_y(x)$ and the electric field $E_y(x)$ of the electromagnetic wave:

$$P_y(x) = 8\pi M_0^2 \sum_{k,l,n,m} \psi_{ek}(x)\psi_{hl}(x) \frac{|G_{n,m}(k_z r_B)|^2}{\varepsilon_{k,l,n,m} - \hbar(\omega + i\nu)} \times \int_0^{d_c} \psi_{ek}^*(x')\psi_{hl}^*(x')E_y(x')dx'. \quad (\text{A5})$$

Here, the asterisk stands for complex conjugation.

As one can see, Eq. (A5) contains the electron/hole eigenfunctions, $\psi_{ek}(x)$ and $\psi_{hl}(x)$, of Hamiltonians \mathcal{H}_{jx} , Eq. (A1). They have different values depending on which region of semiconductor slab c the electron/hole is located: inside the cap-layer barrier ($0 < x < x_1$), inside the QW ($x_1 < x < x_2$), or inside the buffer-layer barrier ($x_2 < x < d_c$), see Fig. 1,

$$\psi_{jk} = \begin{cases} 2A_{jk} \sinh(\Theta_k^j x), & 0 < x < x_1 \\ B_{jk} e^{iK_k^j x} + C_{jk} e^{-iK_k^j x}, & x_1 < x < x_2 \\ 2D_{jk} e^{-\Theta_k^j d_c} \sinh[\Theta_k^j (d_c - x)], & x_2 < x < d_c. \end{cases} \quad (\text{A6})$$

The discrete wave numbers K_k^j and Θ_k^j in the QW and its barriers, respectively, meet the standard definition via the corresponding energy levels E_k^j of the spatial quantization of electron and hole:

$$K_k^j = \sqrt{2m_{jx}E_k^j}/\hbar, \quad \Theta_k^j = \sqrt{2m_{jx}(V_0^j - E_k^j)}/\hbar. \quad (\text{A7})$$

The amplitudes A_{jk} , B_{jk} , C_{jk} , D_{jk} and the eigenenergies E_k^j are numerically calculated from the set of homogeneous equations which are conventionally obtained from the boundary conditions of continuity for ψ_{jk} and its derivative at the QW interfaces $x_j = x_1$ and $x_j = x_2$ and normalizing the respective eigenfunction. In particular, the eigenenergies E_k^j are derived from transcendental dispersion relation:

$$\frac{K_k^j}{\Theta_k^j} \tanh[\Theta_k^j (d_c - x_2)] = \frac{\cos[K_k^j (x_2 - x_1)] + \frac{\Theta_k^j}{K_k^j} \coth[\Theta_k^j x_1] \sin[K_k^j (x_2 - x_1)]}{\sin[K_k^j (x_2 - x_1)] - \frac{\Theta_k^j}{K_k^j} \coth[\Theta_k^j x_1] \cos[K_k^j (x_2 - x_1)]}. \quad (\text{A8})$$

The function $G_{n,m}(k_z r_B)$ is directly related to the eigenfunction of the bidimensional Hamiltonian \mathcal{H}_{2D} , Eq. (A2), providing quantization of the electron-hole pair state by the external dc magnetic field \mathbf{B}_0 :

$$G_{n,m}(k_z r_B) = \frac{(2\pi)^{-1/2}}{r_B} \left(\frac{n!}{2^{|m|}(n+|m|)!} \right)^{1/2} e^{i\pi m/2} \times (k_z r_B)^{|m|} L_n^{|m|} [(k_z r_B)^2/2] e^{-(k_z r_B)^2/4}. \quad (\text{A9})$$

The characteristic magnetic length r_B is defined by

$$r_B = (c\hbar/eB_0)^{1/2}, \quad (\text{A10})$$

and $L_n^{|m|}$ represents the associated Laguerre polynomials. In accordance with Eq. (A9), the quantum number $m = 0, \pm 1, \pm 2, \pm \dots$ defines the angular momentum of the exciton center-of-mass along the magnetic field \mathbf{B}_0 . Both quantum numbers $n = 0, 1, 2, \dots$ and m determine the Landau levels corresponding to the relative motion of the electron-hole pair in the QW plane as follows from the expression for the total quantum magnetoexciton energy $\varepsilon_{k,l,n,m}$:

$$\varepsilon_{k,l,n,m} = E_g + E_k^e + E_l^h + \hbar\omega_c \left[n + \frac{1}{2}(m\gamma + |m| + 1) \right]; \quad \omega_c = \frac{eB_0}{c\mu}, \quad \mu = \frac{m_{e\parallel}m_{h\parallel}}{m_{e\parallel} + m_{h\parallel}}, \quad \gamma = \frac{m_{h\parallel} - m_{e\parallel}}{m_{e\parallel} + m_{h\parallel}}, \quad (\text{A11})$$

with the magnetoexciton cyclotron frequency ω_c containing the reduced excitonic mass μ .

In this paper, for definiteness, we consider the effect of magnetoexcitons whose electrons and holes occupy the lowest levels of the spatial quantization, respectively, with quantum numbers $k = 1$ and $l = 1$. In such a case, Eq. (A5) for the polarization transforms into

$$P_y(x) = 8\pi M_0^2 \sum_{n,m} \psi_{e1}(x)\psi_{h1}(x) \frac{|G_{n,m}(k_z r_B)|^2}{\varepsilon_{1,1,n,m} - \hbar(\omega + i\nu)} \times \int_0^{d_c} \psi_{e1}^*(x')\psi_{h1}^*(x')E_y(x')dx', \quad (\text{A12})$$

which significantly simplifies the problem. Indeed, the integral Eq. (2.12) for the electric field $E_y(x)$ with $P_y(x)$ in the form of Eq. (A12) is readily resolved, giving rise to the analytical expressions (2.16) for the electric and magnetic fields. The introduced functions, $I(x)$ and $J(x)$, are defined by

$$I(x) = \frac{k^2}{k_c} W D_1 \left(1 + \frac{k^2}{k_c} W V \right)^{-1} \sin(k_c d_c) \mathfrak{F}(x), \quad (\text{A13a})$$

$$J(x) = \frac{k^2}{k_c} W D_2 \left(1 + \frac{k^2}{k_c} W V \right)^{-1} \sin(k_c d_c) \mathfrak{F}(x), \quad (\text{A13b})$$

$$\mathfrak{F}(x) = \int_0^x \psi_{e1}(x')\psi_{h1}(x') \sin[k_c(x - x')] dx' + \frac{\cos(k_c x)}{\sin(k_c d_c)} \int_0^{d_c} \psi_{e1}(x')\psi_{h1}(x') \cos[k_c(d_c - x')] dx', \quad (\text{A13c})$$

with following auxiliary notations:

$$W = 8\pi M_0^2 \sum_{n,m} \frac{|G_{nm}(k_z r_B)|^2}{\varepsilon_{1,1,n,m} - \hbar(\omega + i\nu)}; \quad (\text{A14a})$$

$$V = \int_0^{d_c} \psi_{e1}^*(x)\psi_{h1}^*(x) \mathfrak{F}(x) dx; \quad (\text{A14b})$$

$$D_1 = \int_0^{d_c} \psi_{e1}^*(x)\psi_{h1}^*(x) \cos[k_c(d_c - x)] dx; \quad (\text{A14c})$$

$$D_2 = \int_0^{d_c} \psi_{e1}^*(x)\psi_{h1}^*(x) \cos(k_c x) dx. \quad (\text{A14d})$$

Note that $I'(0) = J'(0) = 0$ and $I'(d_c) = J'(d_c) = 0$ by definition (A13), providing the identity of Eq. (2.16b) at borders $x = 0$ and $x = d_c$.

The values of functions $I(x)$ and $J(x)$ at $x = 0$ and $x = d_c$ determine the matrix $\hat{\zeta}$ of surface impedances (2.17), (2.18). According to Eqs. (A13) and (A14), such values read

$$I(0) = \frac{k^2}{k_c} W |D_1|^2 \left(1 + \frac{k^2}{k_c} WV\right)^{-1}, \quad (\text{A15a})$$

$$I(d_c) = \frac{k^2}{k_c} W D_1 D_2^* \left(1 + \frac{k^2}{k_c} WV\right)^{-1}, \quad (\text{A15b})$$

$$J(0) = \frac{k^2}{k_c} W D_1^* D_2 \left(1 + \frac{k^2}{k_c} WV\right)^{-1}, \quad (\text{A15c})$$

$$J(d_c) = \frac{k^2}{k_c} W |D_2|^2 \left(1 + \frac{k^2}{k_c} WV\right)^{-1}. \quad (\text{A15d})$$

-
- [1] J. A. Hutchison, A. Liscio, T. Schwartz, A. Canaguier-Durand, C. Genet, V. Palermo, P. Samorì, and T. W. Ebbesen, *Adv. Mater.* **25**, 2481 (2013).
- [2] A. Frisk Kockum, A. Miranowicz, S. De Liberato, S. Savasta, and F. Nori, *Nat. Rev. Phys.* **1**, 19 (2019).
- [3] Y. Yamamoto, *Coherence, Amplification, and Quantum Effects in Semiconductor Laser* (Wiley, New York, 1991), Chap. 13, p. 561.
- [4] V. Savona, L. C. Andreani, P. Schwendimann, and A. Quattropani, *Solid State Commun.* **93**, 733 (1995).
- [5] Y. Zhu, D. J. Gauthier, S. E. Morin, Q. Wu, H. J. Carmichael, and T. W. Mossberg, *Phys. Rev. Lett.* **64**, 2499 (1990).
- [6] C. Weisbuch, M. Nishioka, A. Ishikawa, and Y. Arakawa, *Phys. Rev. Lett.* **69**, 3314 (1992).
- [7] G. Panzarini, L. C. Andreani, A. Armitage, D. Baxter, M. S. Skolnick, V. N. Astratov, J. S. Roberts, A. V. Kavokin, M. R. Vladimirova, and M. A. Kaliteevski, *Phys. Solid State* **41**, 1223 (1999).
- [8] R. Houdré, *Phys. Status Solidi B* **242**, 2167 (2005).
- [9] B. Deveaud, *The Physics of Semiconductor Microcavities* (Wiley-VCH, Weinheim, 2007).
- [10] H. M. Gibbs, G. Khitrova, and S. W. Koch, *Nat. Photonics* **5**, 275 (2011).
- [11] J. B. Khurgin, *Solid State Commun.* **117**, 307 (2001).
- [12] D. S. Citrin and J. B. Khurgin, *Phys. Rev. B* **68**, 205325 (2003).
- [13] A. Vasanelli, Y. Todorov, and C. Sirtori, *C. R. Phys.* **17**, 861 (2016).
- [14] C. R. Gubbin, S. A. Maier, and S. Kéna-Cohen, *Appl. Phys. Lett.* **104**, 233302 (2014).
- [15] G. Scalari, C. Maissen, D. Turcinková, D. Hagenmüller, S. De Liberato, C. Ciuti, D. Schuh, C. Reichl, W. Wegscheider, M. Beck, and J. Faist, *Science* **335**, 1323 (2012).
- [16] T. Niemczyk, F. Deppe, H. Huebl, E. P. Menzel, F. Hocke, M. J. Schwarz, J. J. Garcia-Ripoll, D. Zueco, T. Hümmer, E. Solano, A. Marx, and R. Gross, *Nat. Phys.* **6**, 772 (2010).
- [17] P. A. Hobson, W. L. Barnes, D. G. Lidzey, G. A. Gehring, D. M. Whittaker, M. S. Skolnick, and S. Walker, *Appl. Phys. Lett.* **81**, 3519 (2002).
- [18] A. Macridin, M. Jarrell, T. Maier, P.R.C. Kent, and E. D'Azevedo, *Phys. Rev. Lett.* **97**, 036401 (2006).
- [19] M. Oda, K. Hirata, T. Inoue, Y. Obara, T. Fujimura, and T. Tani, *Phys. Status Solidi C* **6**, 288 (2009).
- [20] T. Schwartz, J. A. Hutchison, C. Genet, and T. W. Ebbesen, *Phys. Rev. Lett.* **106**, 196405 (2011).
- [21] G. H. Lodden and R. A. Holmes, *Appl. Phys. Lett.* **98**, 233301 (2011).
- [22] T. Ellenbogen, P. Steinvurzel, and K. B. Crozier, *Appl. Phys. Lett.* **98**, 261103 (2011).
- [23] C. Brimont, L. Doyennette, G. Kreyder, F. Réveret, P. Disseix, F. Médard, J. Leymarie, E. Cambriil, S. Bouchoule, M. Gromovyi, B. Alloing, S. Rennesson, F. Semond, J. Zúñiga-Pérez, and T. Guillet, *Phys. Rev. Appl.* **14**, 054060 (2020).
- [24] P. M. Walker, L. Tinkler, M. Durska, D. M. Whittaker, I. J. Luxmoore, B. Royall, D. N. Krizhanovskii, M. S. Skolnick, I. Farrer, and D. A. Ritchie, *Appl. Phys. Lett.* **102**, 012109 (2013).
- [25] J. Ciers, J. G. Roch, J. F. Carlin, G. Jacopin, R. Butté, and N. Grandjean, *Phys. Rev. Appl.* **7**, 034019 (2017).
- [26] R. Yan, D. Gargas, and P. Yang, *Nat. Photonics* **3**, 569 (2009).
- [27] P. Paniagua-Domínguez, R. Grzela, J. Gómez-Rivas, and J. A. Sánchez-Gil, *Nanoscale* **5**, 10582 (2013).
- [28] D. R. Abujetas, J. Feist, F. J. García-Vidal, J. G. Rivas, and J. A. Sánchez-Gil, *Phys. Rev. B* **99**, 205409 (2019).
- [29] J. Wilkes and E. A. Muljarov, *Phys. Rev. B* **94**, 125310 (2016).
- [30] P. L. Valdés-Negrin, B. Flores-Desirena, M. Toledo-Solano, and F. Pérez-Rodríguez, *AIP Adv.* **10**, 065223 (2020).
- [31] S. S. Apostolov, N. M. Makarov, and V. A. Yampol'skii, *Phys. Rev. B* **97**, 024510 (2018).
- [32] N. Kvitka, S. S. Apostolov, N. M. Makarov, T. Rokhmanova, A. A. Shmat'ko, and V. A. Yampol'skii, *Phys. Rev. B* **103**, 104512 (2021).
- [33] S. Cortés-López and F. Pérez-Rodríguez, *Low Temp. Phys.* **46**, 531 (2020).
- [34] A. Stahl and I. Balslev, *Electrodynamics of the Semiconductor Band Edge* (Springer, Berlin, Heidelberg, 1987).
- [35] S. Zielińska-Raczyńska, D. A. Fishman, C. Faugeras, M. M. P. Potemski, P. H. M. van Loosdrecht, K. Karpiński, G. Czajkowski, and D. Ziemkiewicz, *New J. Phys.* **21**, 103012 (2019).
- [36] D. Ziemkiewicz, G. Czajkowski, K. Karpiński, and S. Zielińska-Raczyńska, *Phys. Rev. B* **103**, 035305 (2021).
- [37] B. Flores-Desirena and F. Pérez-Rodríguez, *J. Appl. Phys.* **109**, 014303 (2011).
- [38] S. Artyukhin, D. Fishman, C. Faugeras, M. Potemski, A. Revcolevschi, M. Mostovoy, and P. H. van Loosdrecht, *Sci. Rep.* **8**, 7818 (2018).
- [39] E. Shkondin, O. Takayama, M. E. Aryaee Panah, P. Liu, P. V. Larsen, M. D. Mar, F. Jensen, and A. V. Lavrinenko, *Opt. Mater. Express* **7**, 1606 (2017).
- [40] M. A. Green, *Sol. Energy Mater. Sol. Cells* **92**, 1305 (2008).
- [41] M. Spotnitz, N. H. Kwong, and R. Binder, *Phys. Rev. B* **104**, 115305 (2021).

- [42] N. A. Gippius, A. L. Yablonskii, A. B. Dzyubenko, S. G. Tikhodeev, L. V. Kulik, V. D. Kulakovskii, and A. Forchel, *J. Appl. Phys.* **83**, 5410 (1998).
- [43] S. V. Zhukovsky, A. Andryieuski, O. Takayama, E. Shkondin, R. Malureanu, F. Jensen, and A. V. Lavrinenko, *Phys. Rev. Lett.* **115**, 177402 (2015).
- [44] S. Jahani and Z. Jacob, *IEEE Photonics J.* **7**, 0700505 (2015).
- [45] S. Jahani and Z. Jacob, *Optica* **1**, 96 (2014).
- [46] G. Czajkowski and A. Tredicucci, *Il Nuovo Cimento D* **14**, 1203 (1992).